fractal and fractional

MDPI

Article

Fractal Characteristics of Pore Structure Evolution in Unconsolidated Sandstones Under Prolonged Water Injection

Hongzhu Li [1,2], Haifeng Lyu [3], Zhaobo Gong [4], Taotao Song [4], Weiyao Zhu [1,2] and Debin Kong [1,2,*]

[1] China-Zambia Belt and Road Joint Laboratory on Green and Safe Development of Mineral Resources, University of Science and Technology Beijing, Beijing 100083, China
[2] School of Resource and Safety Engineering, University of Science and Technology Beijing, Beijing 100083, China
[3] Development Division, Petro China Xinjiang Oilfield Company, Karamay 834000, China
[4] Branch Supervision Center of Xinjiang Oilfield Co., Ltd., China National Petroleum Corporation, Karamay 834000, China
* Correspondence: kongdb@ustb.edu.cn

Abstract

Prolonged water injection in unconsolidated sandstone reservoirs can induce pore rearrangement and modify flow pathways, thereby affecting reservoir performance. However, quantitative characterization of pore evolution in both temporal and spatial dimensions remains limited. This study investigates the mechanisms of pore-structure evolution during extended injection through a series of multi-scale experiments. Scanning electron microscopy and X-ray diffraction analyses were employed to compare mineral composition and microstructural characteristics before and after injection, while in situ nuclear magnetic resonance (NMR) monitoring captured the dynamic evolution process, enabling pore-size classification from T_2 spectra and fractal assessment of structural complexity. Segmented NMR measurements at different distances further resolved spatial heterogeneity. The results show that prolonged water injection reduced permeability by 10.4–32.1%, whereas porosity exhibited only minor variation, indicating that the decline in flow capacity is primarily controlled by pore–throat structural adjustment rather than pore volume loss. Mineralogical redistribution and fine-particle migration decreased the median pore radius by 21.5–51.8% and the micropore fractal dimension by 23.8–76.5%, with stronger responses observed at higher permeabilities, while meso- and macropore fractal dimensions remained nearly unchanged, indicating preferential modification of micropores with preservation of the main connected flow framework. Consistently, NMR responses reveal pronounced spatial heterogeneity along the flow direction. The NMR signal changes at the injection end were 11.2–18.4% and 7.7–21.7% during the early and intermediate stages, respectively, both exceeding those at the distal end (2.9–12.4% and 1.9–17.1%). These results indicate a downstream-attenuating structural modification gradient. The findings provide new insights into pore-structure evolution during prolonged water injection and offer a scientific basis for optimizing water-injection strategies in unconsolidated sandstone reservoirs.

Keywords: fractal theory; hydrocarbon reservoirs; unconsolidated sandstone; prolonged water injection; pore structure evolution

Check for updates

Academic Editor: Kouqi Liu

Received: 22 February 2026
Revised: 18 March 2026
Accepted: 19 March 2026
Published: 21 March 2026

Copyright: © 2026 by the authors. Licensee MDPI, Basel, Switzerland. This article is an open access article distributed under the terms and conditions of the Creative Commons Attribution (CC BY) license.

1. Introduction

As major reservoirs for hydrocarbon storage, unconsolidated sandstones are of great economic value and engineering relevance in oil and gas exploitation [1–4]. Water injection,

a conventional and effective method for pressure maintenance and reservoir management, can trigger pore-structure reorganization and the evolution of seepage pathways within these formations [5–7]. Such changes may negatively influence injection–production performance, reduce well-pattern adaptability, and increase both operational risks and economic costs. Therefore, a comprehensive evaluation of both the macroscopic porosity–permeability response and the microscopic pore-structure evolution during water injection is crucial for improving recovery performance and optimizing development strategies in unconsolidated sandstone reservoirs.

Among the available non-destructive characterization methods, nuclear magnetic resonance (NMR) and computed tomography (CT) scanning have been extensively employed to investigate pore–throat structures in reservoir rocks [8–11]. NMR provides an effective means to evaluate pore-size distribution at various displacement stages in the same core while maintaining high sensitivity to dynamic changes [12–15]. Because NMR-based pore characterization depends on the inversion of relaxation signals, the resulting parameters cannot directly reproduce the actual pore morphology or geometric configuration. In addition, the correlation between transverse relaxation time (T_2) and pore size generally requires calibration through independent experimental measurements [16,17]. Micro–CT imaging, by contrast, is capable of generating high-resolution three-dimensional representations of pore–throat systems at the pore scale. When combined with digital rock reconstruction techniques [18], these datasets allow the extraction of diverse geometric and topological descriptors, providing valuable quantitative constraints for evaluating reservoir storage capacity and interpreting displacement processes. Nevertheless, the relatively high experimental cost and limited imaging throughput of CT restrict its application in continuous monitoring during long-term displacement experiments. Furthermore, destructive analytical methods, including scanning electron microscopy (SEM) and X-ray diffraction (XRD), can deliver detailed information on mineralogical composition and surface morphology at the microscale, yet they are inherently incapable of capturing temporal evolution during ongoing flow processes. Integrating these destructive techniques with non-destructive approaches such as NMR and CT therefore enables the establishment of a multiscale pore-structure characterization framework, which supports a more systematic interpretation of pore evolution mechanisms during water injection in unconsolidated sandstones.

Although conventional experiments yield rich pore-scale statistics and three-dimensional imagery, they seldom provide a unified, multiscale descriptive framework for systematically assessing pore complexity and spatial heterogeneity. To fill this gap, fractal analysis has been adopted as a mathematical approach for quantifying multiscale irregularity [19,20]. By fitting pore-size or pore-volume distributions (or cumulative T_2 spectra) in log–log coordinates, the fractal dimension furnishes quantitative measures of heterogeneity, scale extent and connectivity changes and thus serves as an indicator of pore-structure evolution induced by water injection [21]. Nonetheless, fractal metrics are contingent on model assumptions and segmentation schemes and are typically inferred from indirect proxies such as NMR or mercury-intrusion data; this limits their ability to directly reconstruct three-dimensional pore morphology and necessitates validation against complementary observations when relating fractal measures to flow behavior. Unconsolidated sandstones exhibit complex pore-structure changes during prolonged water-injection development, yet existing studies mostly provide single-point descriptions, lacking systematic, multi-dimensional quantitative analyses of pore-evolution. To address this issue, multi-scale experimental investigations were carried out to reveal the mechanisms controlling pore-structure evolution in unconsolidated sandstones under prolonged water injection conditions. First, SEM and XRD are used to compare mineralogy and micro-morphology before and after water injection. Second, online NMR is employed to monitor pore-and-permeability char-

acteristics in real time throughout the prolonged injection process; based on the T_2 spectra, pore sizes are quantitatively classified and fractal dimensions are calculated to characterize the complexity changes in pore structures at different scales. In parallel, the total NMR signal is analyzed in segmented intervals at different distances from the injection inlet to capture the spatially heterogeneous response of pore structure to prolonged injection. This work provides a reliable reference for elucidating the evolution patterns of pore structure in unconsolidated sandstone reservoirs under prolonged water-injection conditions.

2. Materials and Methods

2.1. Equipment and Materials

Core-scale water injection tests were carried out using a multiphase flow system developed for porous media investigations. The mineralogical composition of the samples was characterized through XRD analysis performed with an Ultima IV diffractometer (Rigaku Corporation, Tokyo, Japan) following the SY/T 5163-2018 standard [22]. Microstructural features were further analyzed using SEM on a JSM-5500LV instrument (JEOL Ltd., Tokyo, Japan). In addition, T_2 relaxation measurements were obtained using a MesoMR3-060H-I NMR system (Newmai Company, Suzhou, China). Synthetic formation brine was prepared by dissolving NaCl and KCl in water, resulting in a total salinity of 31,367.7 mg/L. The fundamental properties of the core samples, together with the initial whole-rock mineral composition and the relative abundance of clay minerals, are listed in Tables 1–3.

Table 1. Physical and petrophysical properties of the core samples.

Cores	Length (cm)	Diameter (cm)	Porosity (%)	Air Permeability (mD)
#1	5.2	2.46	20.33	94.25
#2	5.42	2.37	28.55	1173.73
#3	5.3	2.40	28.95	2599.89
#4	5.211	2.424	14.05	5504.67

Note: "#" denotes the core sample identification number.

Table 2. Initial whole-rock mineral content.

Cores	Contents (%)				
	Total Clay Minerals	Quartz	K-Feldspar	Plagioclase	Others
#1	24.6	55.1	2.9	16	1.4
#2	10.8	52.4	7.9	26.4	2.5
#3	9.3	44.5	9.4	31.0	5.8
#4	5.3	46.1	10.0	14.2	24.4

Note: "#" denotes the core sample identification number.

Table 3. Initial relative content of clay minerals.

Cores	Relative Contents (%)			
	Kaolinite	Chlorite	Illite	Illite/Smectite Mixed Layer
#1	29.6	19.6	8.3	42.5
#2	11.2	17.8	14.5	56.5
#3	11.7	32.1	11.8	44.4
#4	7.1	12.9	45.5	34.5

Note: "#" denotes the core sample identification number.

2.2. Experimental Methods

2.2.1. Measurement of Core Porosity and Permeability

Porosity and permeability analyses were carried out using a PoroPDP-200 overburden porosity–permeability measurement system (Core Laboratories Inc., Houston, TX, USA) in compliance with GB/T 29172-2012 [23]. Nitrogen with a purity of 99.999% was employed as the testing gas. Gas-expansion measurements based on Boyle's law were used to determine porosity. Prior to testing, core plugs were oven-dried and subjected to a confining pressure of 200 psi inside the measurement chamber. The pore volume was subsequently derived from pressure variations associated with gas equilibration. Permeability was evaluated using a non-steady-state pulse-decay approach. A minor pressure perturbation was introduced across the sample, and pressure responses at both inlet and outlet boundaries were continuously monitored. The evolution of differential and mean pressures with time was analyzed in logarithmic form, and permeability was determined from regression analysis of the pressure decay behavior. The application of low-pressure differentials reduced deviations from Darcy flow, while measurements conducted under multiple pore-pressure conditions enabled correction of gas permeability for the Klinkenberg effect.

2.2.2. Scanning Electron Microscopy Analysis

In accordance with the standard SEM analysis procedure for rock samples (SY/T 5162-2021) [24], cleaned and dried core samples were cut into cubic specimens with a side length of approximately 1 cm. The specimen surfaces were sequentially ground with progressively finer sandpapers (from 800 to 2000 mesh) to achieve a smooth and flat finish, followed by argon ion polishing with an oil-based medium to further enhance surface quality. After polishing, the specimens were dried at 60 °C for 4 h and cooled to room temperature. Finally, a thin conductive gold coating was applied to the surfaces prior to microstructural observation using a JSM-5500LV scanning electron microscope (JEOL, Tokyo, Japan).

2.2.3. X-Ray Diffraction Analysis of Whole Rock and Clay Minerals

Mineralogical analysis of clay and non-clay components was conducted following the XRD standard for sedimentary rocks (SY/T 5163-2018) [25]. Prior to analysis, rock samples were dried at 60 °C for 4 h and allowed to cool naturally to ambient temperature. The dried material was subsequently pulverized using an agate mortar until the particle size was reduced to below 40 μm. The powdered samples were then placed into glass holders and carefully flattened to produce a uniform surface suitable for bulk mineral analysis. Whole-rock mineralogy was identified using an Ultima IV X-ray diffractometer (Rigaku, Osaka, Japan). For clay mineral determination, the rock samples were first crushed to a particle size of approximately 1 mm. About 6 g of the crushed material was then dispersed in deionized water and subjected to ultrasonic treatment to enhance particle dispersion. The clay-sized fraction was subsequently isolated through centrifugation at 3000 rpm for 30 min. Prior to separation, hydrogen peroxide was applied when required to eliminate carbonate cement and trace organic matter. The obtained clay suspension was repeatedly rinsed with deionized water and centrifuged until a stable dispersion was achieved. The purified clay fraction was mounted on glass slides and naturally dried to form oriented specimens. Identification and semi-quantitative analysis of clay minerals were finally carried out using X-ray diffraction with an Ultima IV diffractometer.

2.2.4. NMR T_2 Spectra and Pore Size Distribution Analysis

T_2 relaxation measurements of the core samples were performed using a MesoMR3-060H-I nuclear magnetic resonance system (Newmai, Suzhou, China). The instrument operated with a permanent magnetic field of 0.5 ± 0.08 T, corresponding to a resonance frequency of 21.3 MHz. A GR-HSE pulse sequence was adopted, with an echo spacing (TE) of 0.1 ms and a waiting time (TW) of 9000 ms, while 5000 echoes were collected during each acquisition. Under these acquisition settings, the NMR measurements were capable of detecting pore-fluid signals associated with pore sizes ranging approximately from 2 nm to 1 mm. The T_2 values reflect the relaxation behavior of hydrogen nuclei, and their fundamental relationship with pore geometry, when dominated by surface relaxation, can be expressed as:

$$\frac{1}{T_2} = \rho \frac{S}{V_{pore}} \tag{1}$$

In the equation, T_2 denotes the relaxation time, ms; ρ is the surface relaxation rate, μm/s; S and V_{pore} represent the surface area and volume of a single pore, respectively. By adopting a simplified geometric approximation (e.g., nearly spherical pores), one has $S/V_{pore} = c/r$ for a sphere, which leads to an approximately linear relationship between the pore radius r and T_2:

$$r \approx c\rho T_2 r \tag{2}$$

To characterize the self-similar/power-law features of pores at different scales, the cumulative signal intensity in a double-logarithmic coordinate system was used. Power-law fitting was performed for T_2. Let $\sum A(T_2)$ denote the cumulative signal intensity exceeding a certain T_2 value. When the pore sizes follow a power-law distribution and T_2 is approximately proportional to the pore size, a power-law relationship can be established:

$$\sum A(T_2) \propto T_2^{\alpha} \tag{3}$$

In double-logarithmic coordinates:

$$\log \sum A(T_2) = \alpha \log T_2 + C \tag{4}$$

If the commonly used volumetric fractal characterization is adopted (the fractal dimension of the three-dimensional pore space is usually denoted as D, $2 < D < 3$), theoretical and empirical studies provide the relationship between the cumulative signal intensity $\sum A(T_2)$ and the pore size r as $\sum A(T_2) \propto T_2^{3-D}$. Since $T_2 \propto r$, it can be derived that:

$$\alpha = 3 - D \tag{5}$$

Therefore, the fractal dimension D can be inferred from the slope α obtained through fitting:

$$D = 3 - \alpha \tag{6}$$

Based on the fitting results, the relaxation times corresponding to the pore-scale classification are as follows: Core #1—2.19 ms and 84.06 ms; Core #2—2.19 ms and 126.03 ms; Core #3—2.02 ms and 19.56 ms; and Core #4—1.86 ms and 98.84 ms. Using these values, the fractal dimensions D of different pore scales under various water injection multiples were calculated to reveal the differential responses during the displacement process. With increasing fractal dimension, the complexity of the pore structure is significantly enhanced, and the pore-throat network becomes more tortuous. The coordinated evolution of multi-scale fractal parameters provides insight into the changes in pore-scale flow pathways and flow resistance, thereby exerting a pronounced effect on permeability and capillary behavior.

2.2.5. Core-Scale Water Injection Experiments

Core-scale water injection experiments were conducted using sandstone samples with varying initial permeabilities. Prior to the displacement tests, representative fragments were separated from each core for microstructural and mineralogical characterization, including SEM and XRD analyses to determine whole-rock mineralogy and clay mineral composition. The remaining portion of each core was evacuated and subsequently saturated with simulated formation water. After saturation, the initial water permeability of the cores was determined, followed by NMR measurements to acquire the baseline T_2 relaxation spectra of the pore fluids.

For the water injection experiments, the saturated core was installed in a core holder under controlled stress conditions. A confining pressure of 6 MPa was applied, while the outlet boundary was maintained at atmospheric pressure. During injection, the confining pressure was continuously adjusted to remain 1.2 MPa higher than the injection pressure to maintain effective sealing of the core. Water was injected at a constant flow rate of 0.6 mL/min, and the corresponding injection pressure was monitored continuously as a function of the cumulative injected volume. The injection process was continued until either the pressure response stabilized or the injected water volume reached 1000 PV. Core permeability at different stages of water injection was subsequently evaluated based on Darcy's law.

$$K = \frac{5}{3} \times \frac{Q\mu L}{A\Delta p} \tag{7}$$

where $\boldsymbol{K}$ represents the core permeability, mD; $\boldsymbol{Q}$ represents the production rate, mL/min; $\boldsymbol{\mu}$ represents the viscosity of water, mPa·s; $\boldsymbol{L}$ represents the core length, cm; $\boldsymbol{A}$ represents the cross-sectional area of the core, cm^2; $\Delta\boldsymbol{p}$ represents the pressure difference, MPa.

Following completion of the water injection experiments, the core samples were re-examined using SEM and XRD techniques, including analyses of both whole-rock compositions and clay mineral fractions. These post-injection measurements were systematically compared with the corresponding pre-injection data to characterize the evolution of pore architecture and mineralogical features associated with prolonged water injection.

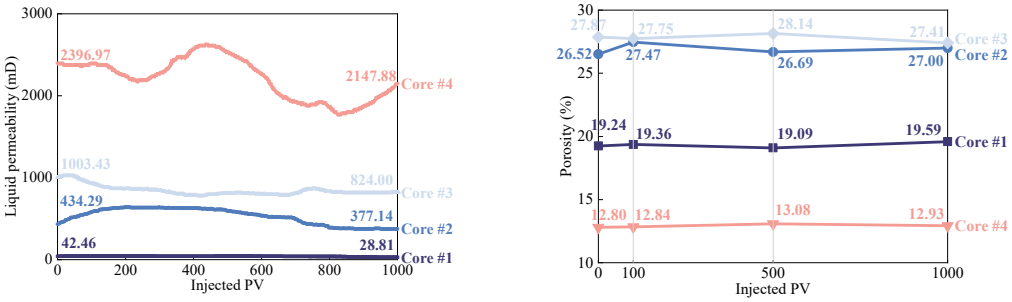
3. Results

3.1. Permeability and Porosity Variations During Prolonged Water Injection

The evolution of liquid permeability was continuously recorded for four unconsolidated sandstone cores in order to investigate how prolonged water injection influences reservoir physical properties at the macroscopic flow scale. The evolution of permeability during water injection is presented in Figure 1a. Core #1 exhibited an initial permeability of 42.46 mD, which gradually decreased with increasing injected pore volume, reaching 28.81 mD at 1000 PV. Core #2 had an initial permeability of 434.29 mD and showed a slight increase during the early stage of injection, followed by a gradual decline to 377.14 mD at 1000 PV. Core #3, with an initial permeability of 1003.43 mD, experienced an initial reduction followed by minor fluctuations, ultimately stabilizing at 824 mD at 1000 PV. Core #4 initially exhibited a fluctuating increase before declining, decreasing from 2396.97 mD to 2147.88 mD at 1000 PV. Overall, all cores exhibited permeability deterioration during prolonged water injection.

Figure 1b illustrates the evolution of NMR-derived porosity for the four cores under prolonged water injection. Overall, the porosity of all cores exhibits only minor variations, indicating that extended water injection has a negligible effect on the total pore volume. Low-porosity cores (Core #1 and Core #4, with initial porosities of approximately 19.2% and 12.8%, respectively) maintain relatively stable porosity throughout the injection process, with only slight fluctuations. In contrast, high-porosity cores (Core #2 and Core #3, with

initial porosities of approximately 26.5% and 27.9%, respectively) experience a minor decrease during the mid-stage of injection, followed by stabilization.



(**a**) (**b**)

Figure 1. Evolution of permeability and NMR-derived porosity during prolonged water injection. (**a**) Permeability; (**b**) NMR-derived porosity. The symbol "#" indicates the identification number of each core sample.

3.2. Changes in Clay Mineral Composition During Prolonged Water Injection

To investigate the evolution of mineral composition under prolonged water injection, a quantitative comparison of bulk mineral contents before and after injection was conducted for four core samples, as shown in Figure 2. Overall, prolonged water injection induced varying degrees of mineralogical alteration in all cores, characterized by a general increase in Quartz content accompanied by reductions in clay minerals and certain feldspar components. For Core #1, the Quartz content increased from 55.1% to 60.0%, while the total clay mineral content decreased from 24.6% to 21.4%. The Plagioclase content showed a slight reduction from 16.0% to 15.5%. In Core #2, Quartz content increased from 52.4% to 56.9%, and total clay minerals decreased from 10.8% to 9.8%. The Plagioclase content declined from 26.4% to 23.9%, whereas K-feldspar exhibited a slight increase. Core #3 displayed a similar trend, with Quartz increasing from 44.5% to 53.8% and Plagioclase decreasing from 31.0% to 26.2%. The total clay mineral content decreased slightly, accompanied by a modest increase in K-feldspar. In Core #4, Quartz content increased from 46.1% to 47.7%, while total clay minerals decreased from 5.3% to 4.9%. Both Plagioclase and minor mineral components exhibited slight reductions, whereas K-feldspar showed a minor increase. Overall, all cores exhibited relative Quartz enrichment and a reduction in clay minerals and portions of feldspar minerals during prolonged water injection.

Given the higher sensitivity of clay minerals to variations in pore structure and flow behavior, a more detailed analysis of clay mineral composition was conducted. The relative abundances of major clay minerals before and after water injection are presented in Figure 3. For Core #1, the Kaolinite content increased from 29.6% to 31.4%, and Chlorite increased from 19.6% to 25.9%, whereas Illite content decreased markedly from 8.3% to 2.6%. The Illite/Smectite mixed-layer (I/S) content showed a slight decrease from 42.5% to 40.1%. In Core #2, Kaolinite and Chlorite contents increased significantly from 11.2% and 17.8% to 25.6% and 38.3%, respectively. Illite content remained nearly unchanged, while the I/S mixed-layer mineral decreased substantially from 56.5% to 21.8%. Core #3 exhibited a different evolutionary pattern, with Kaolinite increasing from 11.7% to 13.4% and the I/S mixed-layer mineral increasing from 44.4% to 49.2%, whereas both Chlorite and Illite contents decreased. In Core #4, Kaolinite and Chlorite contents increased slightly from 7.1% and 12.9% to 7.5% and 14.0%, respectively. Illite content decreased from 45.5% to 31.3%, accompanied by an increase in the I/S mixed-layer mineral from 34.5% to 47.2%. Overall, the responses of clay mineral assemblages to prolonged water injection varied among different cores. However, a general trend of increasing Kaolinite and Chlorite contents was

observed, whereas Illite and I/S mixed-layer minerals exhibited decreasing tendencies in several cores.

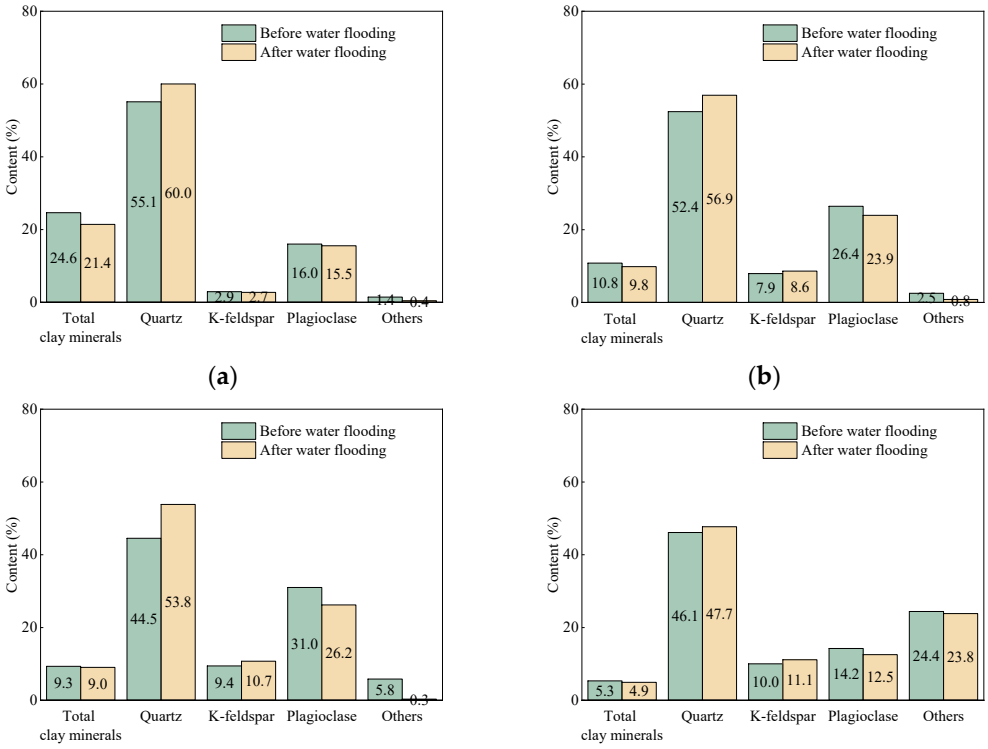


Figure 2. Quantitative analysis of whole-rock minerals. (**a**) Core #1; (**b**) Core #2; (**c**) Core #3; and (**d**) Core #4. The symbol "#" indicates the identification number of each core sample.

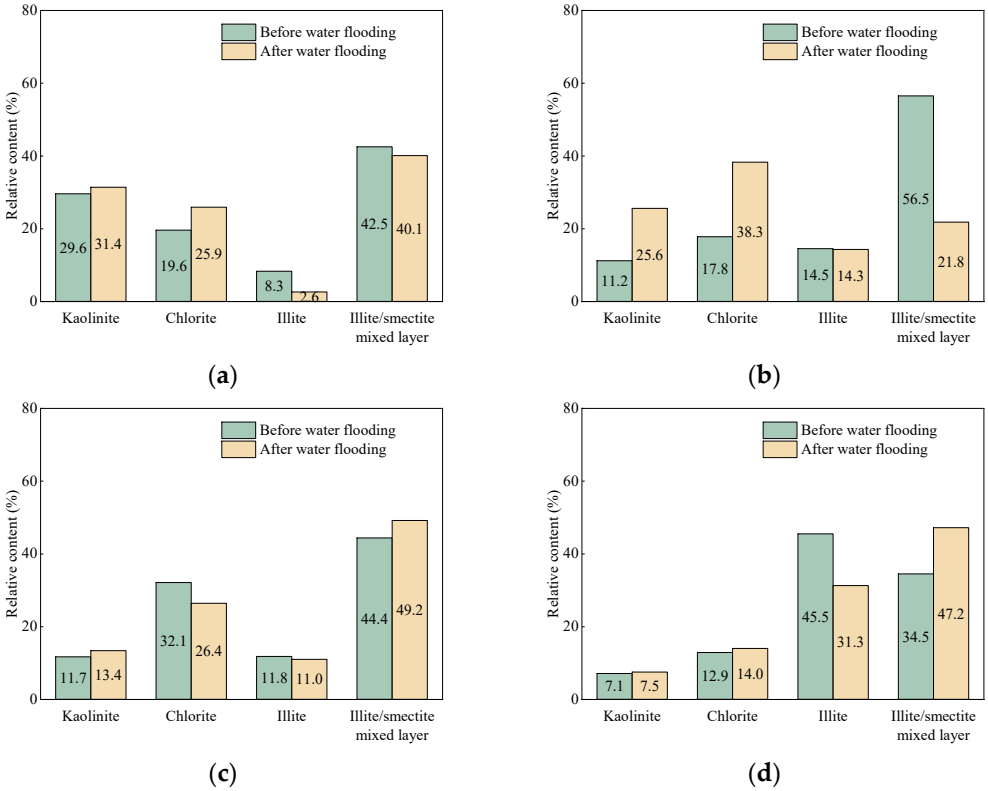


Figure 3. Analysis of relative clay content. (**a**) Core #1; (**b**) Core #2; (**c**) Core #3; and (**d**) Core #4. The symbol "#" indicates the identification number of each core sample.

The variations in bulk mineral composition and clay mineral distribution are further manifested at the microscopic scale as modifications in grain surface morphology and pore–throat structures. Figures 4 and 5 present a comparison of SEM images of the cores before and after prolonged water injection. In Core #1, post-injection observations reveal that platy clay minerals developed coating, bridging, and localized filling features within intergranular pore throats. Meanwhile, secondary minerals were observed adhering to grain surfaces and occupying pore spaces. Grain edges appear smoother than those prior to injection, accompanied by localized dissolution features. Core #2 exhibits microstructural characteristics similar to those of Core #1, where platy clay minerals are distributed along pore-throat surfaces and form bridging structures. Enhanced attachment of secondary minerals is evident on grain surfaces, and accumulations of fine particles are observed within pore spaces. In Core #3, Illite and platy clay minerals are notably more abundant within intergranular pore throats, occurring as film-like coatings and partial fillings. Increased surface attachments are observed on mineral grains, together with discernible edge dissolution features. In Core #4, fibrous and platy clay minerals are markedly reduced after water injection, whereas reaccumulation of fine particles is observed within pore throats. Localized alterations in grain surface morphology and depositional features within pore spaces are also evident. Overall, prolonged water injection resulted in varying degrees of grain surface modification and pore–throat structural adjustment in all cores, primarily characterized by redistribution of clay minerals, enhanced secondary mineral attachment, and localized grain-edge dissolution.

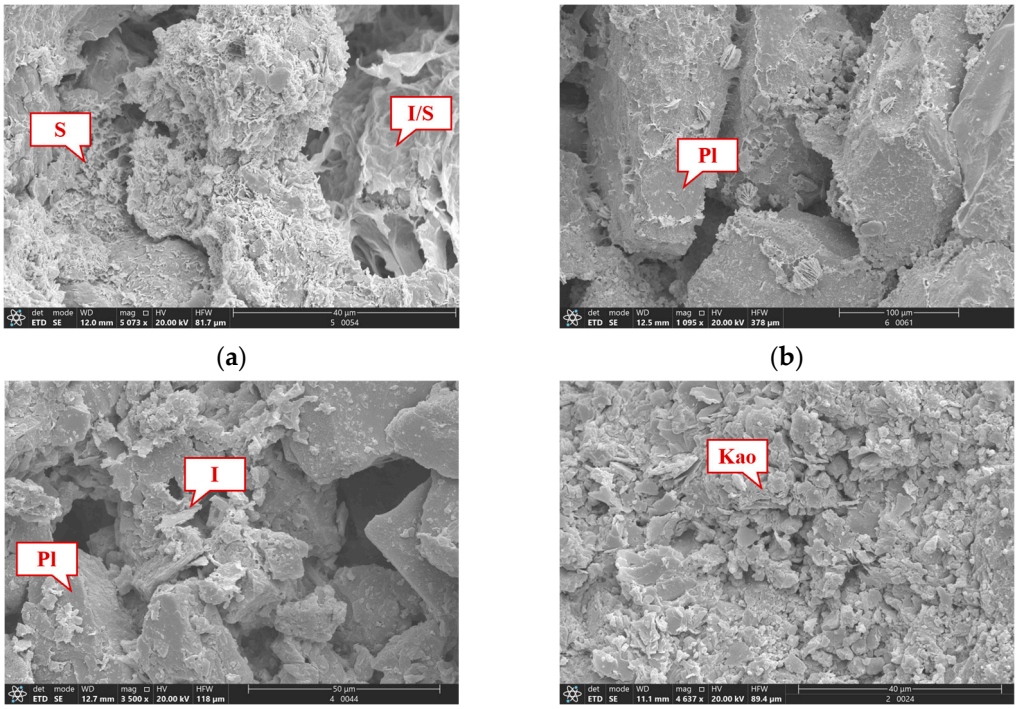


Figure 4. SEM images of all cores before water injection. (**a**) Core #1; (**b**) Core #2; (**c**) Core #3; and (**d**) Core #4. The symbol "#" indicates the identification number of each core sample.

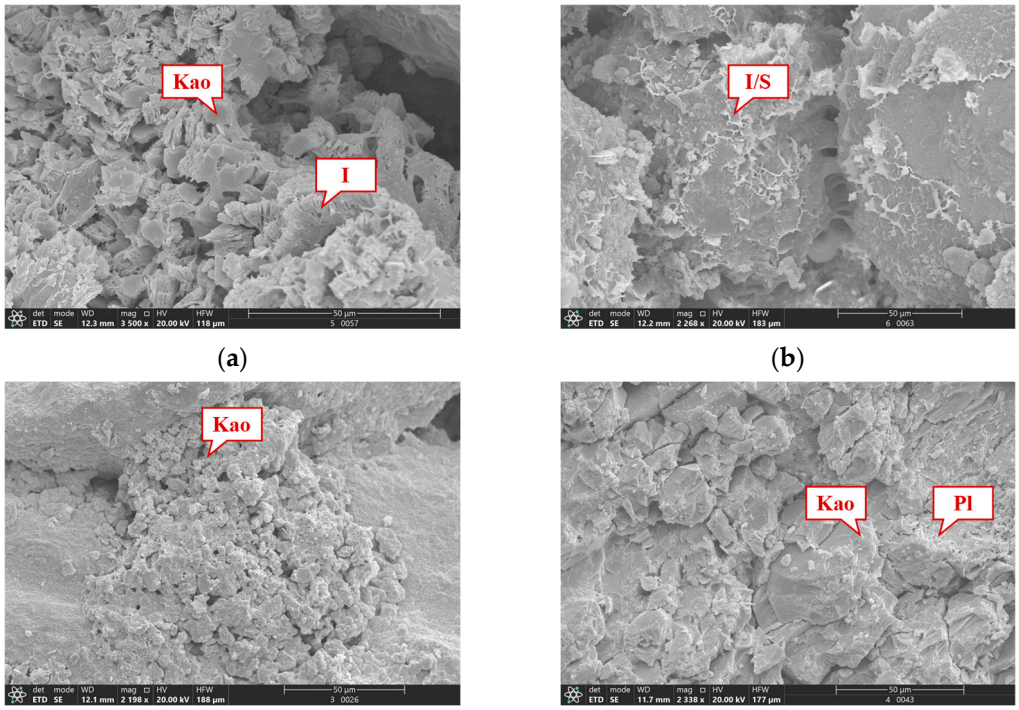


Figure 5. SEM images of all cores after water injection. (**a**) Core #1; (**b**) Core #2; (**c**) Core #3; and (**d**) Core #4. The symbol "#" indicates the identification number of each core sample.

3.3. NMR T_2 Spectral Characteristics During Prolonged Water Injection

To further characterize the dynamic evolution of pore structures during prolonged water injection, NMR measurements were conducted to continuously monitor pore-scale variations in the core samples. Figure 6 presents the evolution of the NMR T_2 distributions for all cores under prolonged water injection. As the injected pore volume increased, the T_2 spectra of all cores exhibited an overall shift toward shorter relaxation times, accompanied by a gradual reduction in signal amplitude within the high-intensity region. This behavior indicates a general transition of pore-size distributions toward smaller scales, suggesting progressive refinement of the pore structure.

Figure 7 further illustrates the evolution of the median pore radius during prolonged water injection. Overall, the median pore radius decreased in all cores with increasing injected pore volume, although the magnitude of reduction varied among samples. For Core #1, the main T_2 peak exhibited only a slight shift with increasing PV, and the median pore radius decreased from 0.535 μm to 0.420 μm, indicating relatively minor structural variation. In Core #2, the median pore radius decreased from 2.830 μm to 1.365 μm, and the T_2 distribution at 1000 PV showed a pronounced deviation from its initial configuration. Core #3 exhibited a reduction in median pore radius from 8.49 μm to 5.22 μm, together with an overall shift of the T_2 spectrum toward shorter relaxation times and a reduction in high-amplitude signals. In Core #4, the T_2 spectrum similarly shifted leftward, with the median pore radius decreasing from 28.60 μm to 22.43 μm. Overall, prolonged water injection resulted in a consistent reduction in pore size and progressive refinement of pore structures across all cores.

To elucidate spatial pore-scale responses along the flow direction, total NMR signals were measured at multiple positions along each core. After data-quality screening, the effective analytical ranges were 20–30 mm (Core #1), 15–30 mm (Core #2), and 15–35 mm (Cores #3–#4). The full T_2 spectra demonstrating the reproducibility and evolution at each position are provided in Appendix A (Figures A1–A4).

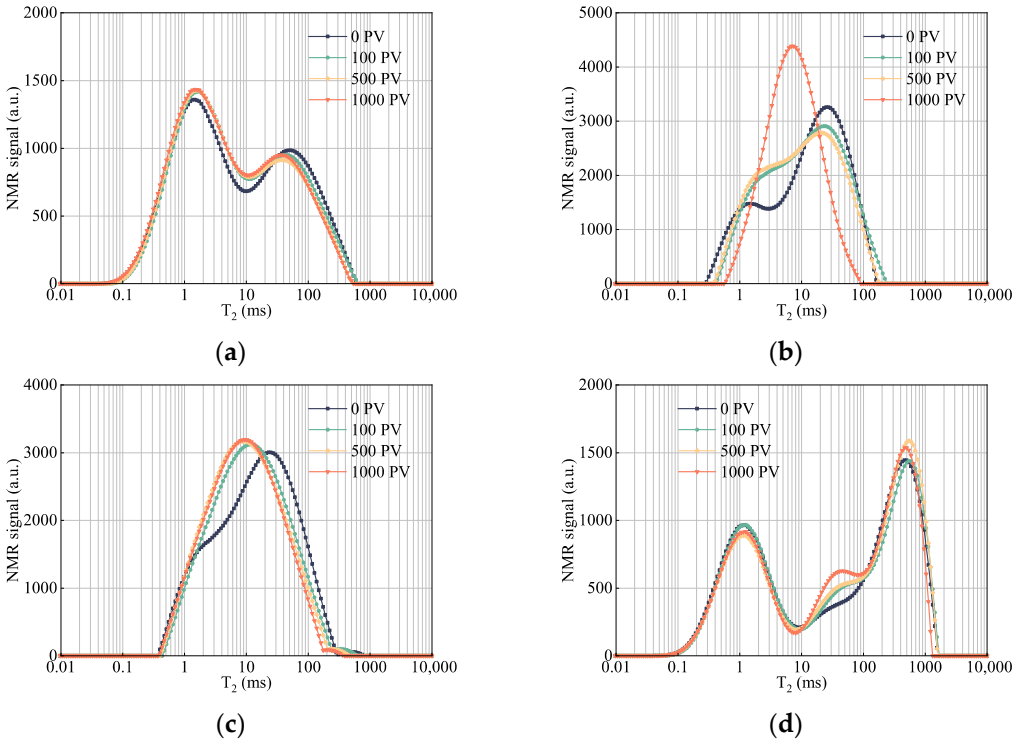


Figure 6. T_2 spectra of four cores. (**a**) Core #1; (**b**) Core #2; (**c**) Core #3; and (**d**) Core #4. The symbol "#" indicates the identification number of each core sample.

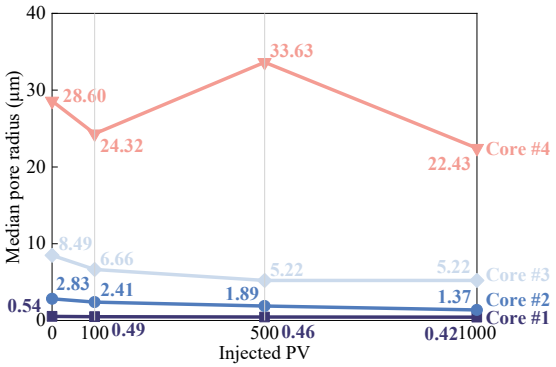


Figure 7. Evolution of median pore radius. The symbol "#" indicates the identification number of each core sample.

4. Discussion

4.1. Mechanisms of Permeability Reduction During Prolonged Water Injection

During prolonged water injection, permeability in all cores exhibited a pronounced declining trend (Figure 1a). The permeability reductions in Core #1, #2, #3, and #4 were 32.1%, 13.2%, 17.9%, and 10.4%, respectively, with the low-permeability core showing a more significant relative deterioration. In contrast, the NMR-derived porosity evolution (Figure 1b) indicates that porosity remained generally stable throughout the injection process, with absolute variations at all stages remaining within 0.5% and no evident monotonic increasing or decreasing trend observed. The coexistence of nearly invariant porosity and continuously declining permeability suggests that the impact of prolonged water injection on reservoir properties is not primarily associated with pore volume loss, but is instead governed by modifications of pore–throat structure and connectivity.

4.2. Evolution of Fractal Characteristics of Pore Structure During Prolonged Water Injection

Under prolonged water injection, the pore structures of loosely consolidated sandstones exhibit distinct responses across different pore-size scales. In this study, by integrating continuous NMR monitoring with pore-scale fractal analysis, the evolution of micropores, mesopores, and macropores during the water injection process was systematically characterized. Figure 8 presents the pore-scale classification of Core #1 and the evolution of pores at different scales during prolonged water injection, while Figure 9 further illustrates the variation in fractal dimensions for each pore scale as a function of injected pore volume. Overall, the structural evolution of Core #1 during prolonged water injection is relatively gradual, and pores at all scales exhibit strong structural stability. D_{micro} decreases progressively from an initial value of 1.076 to 0.82, corresponding to an overall reduction of approximately 23.8%. This trend indicates a certain degree of structural simplification within the micropore system under continuous water injection, where some micropores may have become interconnected or merged due to hydrodynamic flushing. Nevertheless, the evolution remains gradual without abrupt structural transitions, suggesting that the micropore network primarily undergoes progressive adjustment. In contrast, D_{meso} remains highly stable within the range of 2.787–2.800 throughout the injection process, exhibiting only minor fluctuations. This stability indicates that the mesopore structure remains largely unchanged, with only limited local rearrangements occurring during prolonged injection. D_{macro} shows a slight decrease from 2.988 to 2.967 but consistently remains close to 3, implying that the macropore system maintains well-developed three-dimensional connectivity and does not experience significant structural alteration during prolonged water injection. Overall, prolonged water injection in Core #1 primarily induces minor adjustments at the micropore scale, whereas mesopore and macropore structures remain essentially stable, indicating that the dominant flow pathways of this core possess strong structural resilience under prolonged water injection conditions.

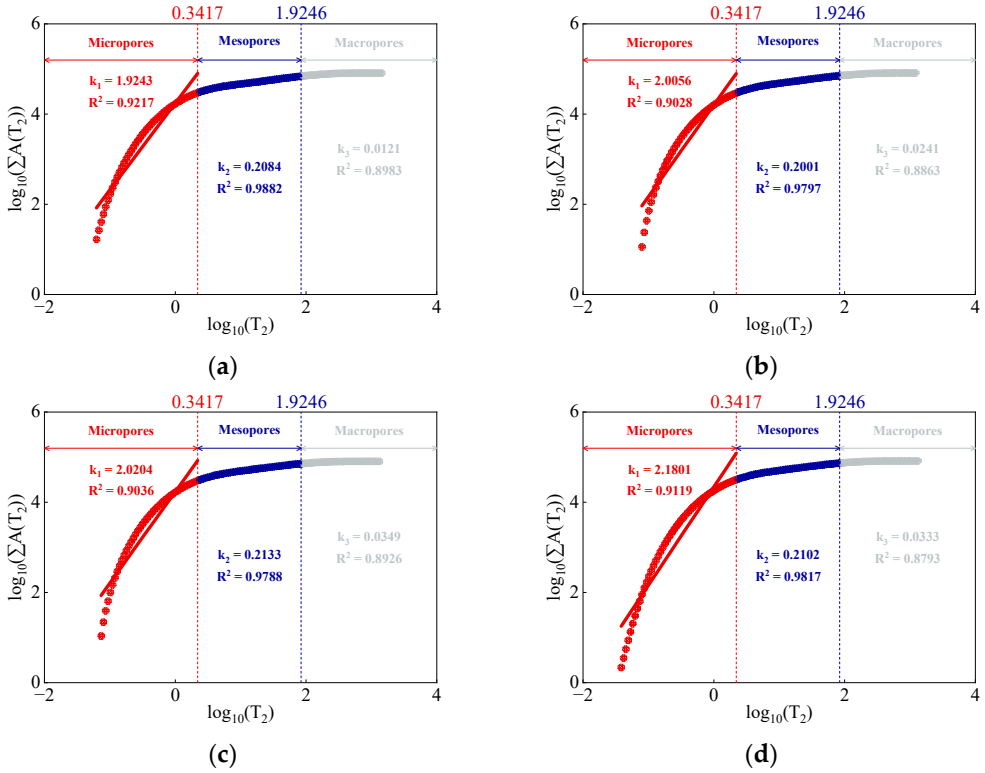


Figure 8. Pore-scale classification and evolution of Core #1. (**a**) 0 PV; (**b**) 100 PV; (**c**) 500 PV; and (**d**) 1000 PV. The symbol "#" indicates the identification number of each core sample.

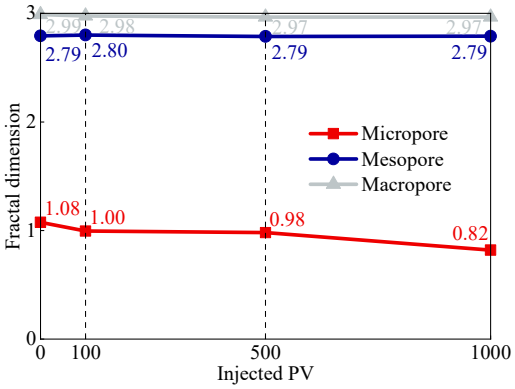


Figure 9. Fractal dimension evolution of multi-scale pores in Core #1. The symbol "#" indicates the identification number of each core sample.

Figure 10 illustrates the pore classification of Core #2 and the evolution of each pore scale during prolonged water injection, while Figure 11 presents the corresponding changes in fractal dimensions across different pore scales. During the injection process, the structural response of Core #2 is predominantly concentrated in the micropores. The initial D_{micro} was 0.81, which rapidly decreased to 0.40 during the early stage and further declined to 0.19 at 1000 PV, representing a reduction of 76.5%. This indicates a continuous weakening of the power-law distribution of micropores, reflecting their erosion, coalescence into larger pore channels, or loss of independent spatial occupancy under prolonged water injection. In the intermediate stage (100–500 PV), minor fluctuations occurred, but the overall decreasing trend persisted; these evolutions correspond to a temporary rearrangement of pre-existing channels during structural adjustment rather than the formation of new pores. In contrast, D_{meso} remained stable within a narrow range of 2.58–2.62, with an evolution of less than 2%, indicating that mesopores underwent only limited restructuring, and their spatial complexity and volumetric distribution were largely preserved. D_{macro} remained close to 3 throughout, suggesting that macropores did not experience fundamental structural modification. Overall, the prolonged water injection predominantly affects the micropores, while the main flow-conducting structures remain essentially unaltered.

Figure 12 illustrates the pore-scale classification of Core #3 and the evolution of each pore scale during prolonged water injection, while Figure 13 presents the corresponding changes in fractal dimension across different pore scales. The fractal responses of pores in Core #3 exhibit characteristic staged evolution. D_{micro} decreases rapidly from 0.54 to 0.21 within 0–100 PV, a reduction of 61.1%, indicating that in the early injection stage, flow is highly concentrated and preferentially mobilizes the pre-existing micropores, leading to a rapid decline in their structural complexity. Subsequently, D_{micro} recovers to 0.30 at 500 PV and stabilizes at 0.25 by 1000 PV, suggesting that the micropore network is not continuously destroyed in the mid-to-late stages; rather, local throat reconnection or flow redistribution reincorporates some previously isolated micropores into the effective connectivity network, resulting in a limited "re-activation" phenomenon. In contrast, D_{meso} exhibits minor evolution, with overall changes less than 3%, indicating that mesopores undergo no significant structural reconfiguration during injection. D_{macro} initially measures 2.87 and rapidly increases to 2.98 during 0–100 PV, maintaining a high, stable level thereafter, reflecting that the main flow pathways are established at an early stage, with subsequent injection primarily optimizing the connectivity of the existing macropore framework rather than generating new pore-scale structures. Similar to the Core #1, the impact of prolonged water injection on the pore structure of Core #2 is also primarily concentrated in the micropores.

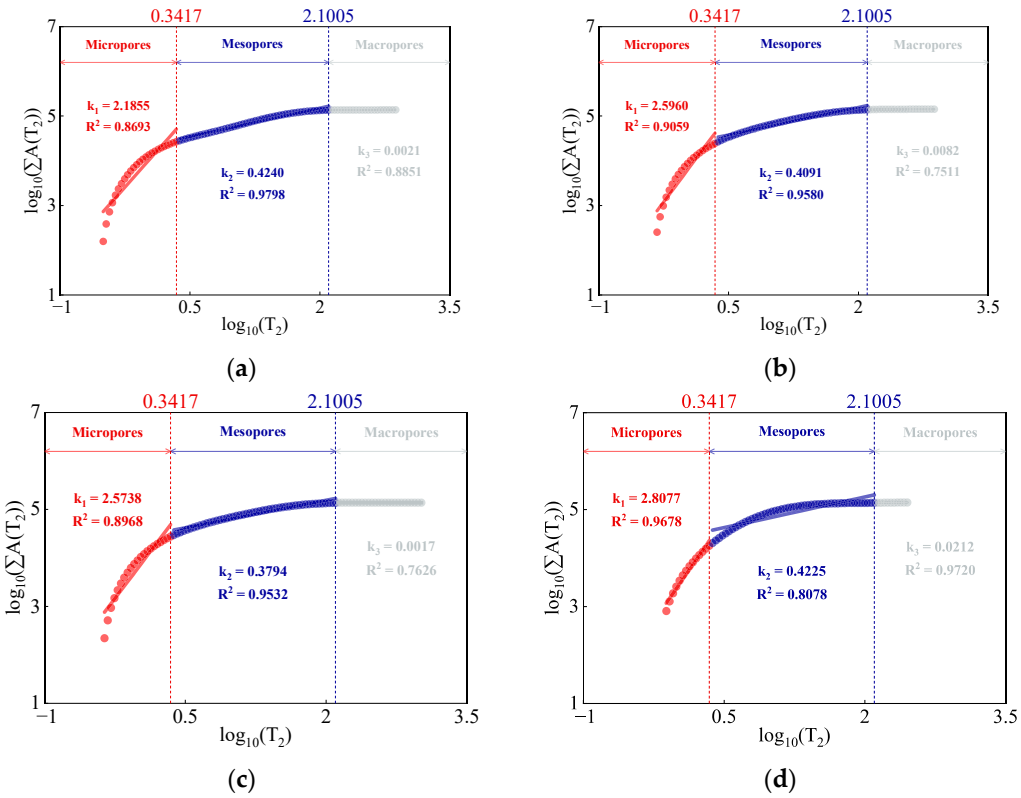


Figure 10. Pore-scale classification and evolution of Core #2. (**a**) 0 PV; (**b**) 100 PV; (**c**) 500 PV; and (**d**) 1000 PV. The symbol "#" indicates the identification number of each core sample.

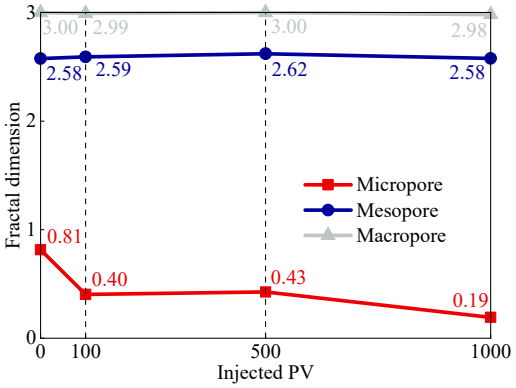


Figure 11. Fractal dimension evolution of multi-scale pores in Core #2.

Figure 14 presents the pore-scale classification of Core #4 and the evolution characteristics of pores at different scales during prolonged water injection, while Figure 15 illustrates the variation in fractal dimensions for each pore scale as a function of injected pore volume. Overall, the structural response of Core #4 to prolonged water injection is primarily concentrated at the micropore scale, whereas mesopore and macropore structures remain generally stable. D_{micro} continuously decreases from an initial value of 0.56 to 0.15, corresponding to a reduction of approximately 73.2%. This pronounced decline indicates a progressive decrease in structural complexity at the micropore scale, suggesting ongoing simplification of the small-pore network during water injection. Such evolution reflects enhanced connectivity or merging of micropores into adjacent flow channels under sustained hydrodynamic flushing, leading to a gradual weakening of the power-law distribution characteristics of the micropore system. Compared with the early injection stage, the rate of decline becomes more gradual during the later stage (500–1000 PV), indicating that structural adjustment progressively approaches a stable state. D_{meso} decreases slightly

from 2.87 to 2.84, with an overall variation of less than 1.5%, suggesting that mesopore structures undergo only limited geometric modification while maintaining overall spatial complexity. D_{macro} fluctuates marginally within the range of 2.80–2.82 without a clear evolutionary trend, indicating that the macropore system preserves a stable connected framework throughout prolonged water injection and does not experience significant structural reconstruction. In summary, prolonged water injection in Core #4 is mainly characterized by continuous simplification of the micropore system, whereas mesopore and macropore structures remain largely unchanged. This behavior suggests that water injection exerts a limited influence on the dominant flow structure of this core, and the overall connectivity framework remains essentially intact.

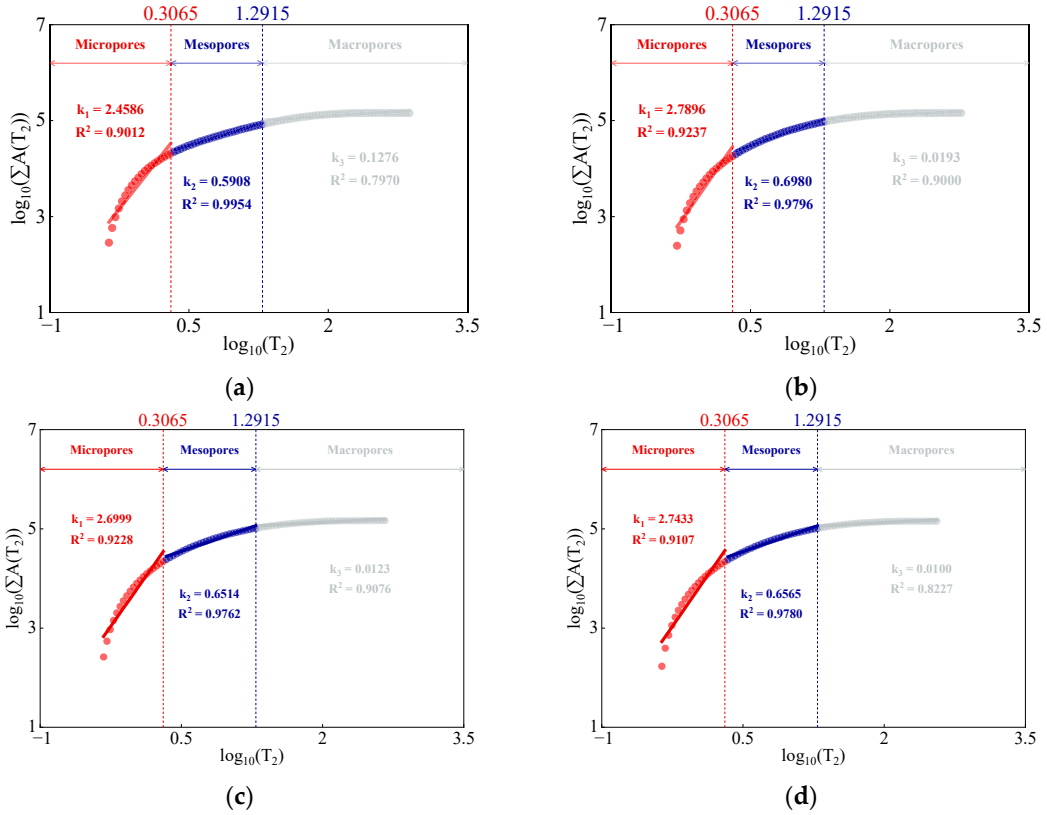


Figure 12. Pore-scale classification and evolution of Core #3. (**a**) 0 PV; (**b**) 100 PV; (**c**) 500 PV; and (**d**) 1000 PV. The symbol "#" indicates the identification number of each core sample.

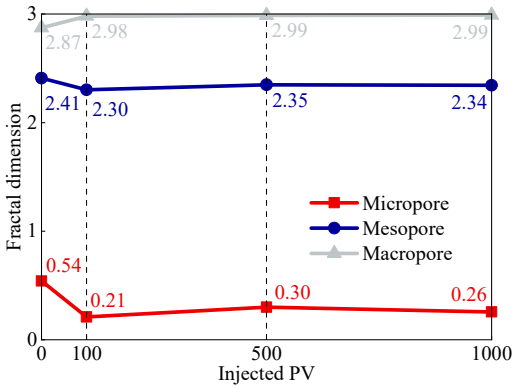


Figure 13. Fractal dimension evolution of multi-scale pores in Core #3. The symbol "#" indicates the identification number of each core sample.

Overall, prolonged water injection primarily affects the micropore system of unconsolidated sandstones, exhibiting a pronounced permeability-dependent response, whereas

the mesopore and macropore structures remain largely stable. Quantitative analysis shows that the D_{micro} values of Core #1, #2, #3, and #4 decrease by 23.8%, 76.5%, 61.1%, and 73.2%, respectively. The magnitude of variation in the D_{micro} increases with permeability, indicating that in higher-permeability cores the micropore system responds more strongly to fluid perturbations during prolonged water injection. In contrast, variations in D_{meso} remain below 3%, suggesting that the mesopore system is largely preserved, with only limited local geometric adjustments. D_{macro} remains close to 3 with only minor fluctuations, indicating that the macropore network consistently maintains a three-dimensional connected framework whose structural stability is essentially independent of permeability.

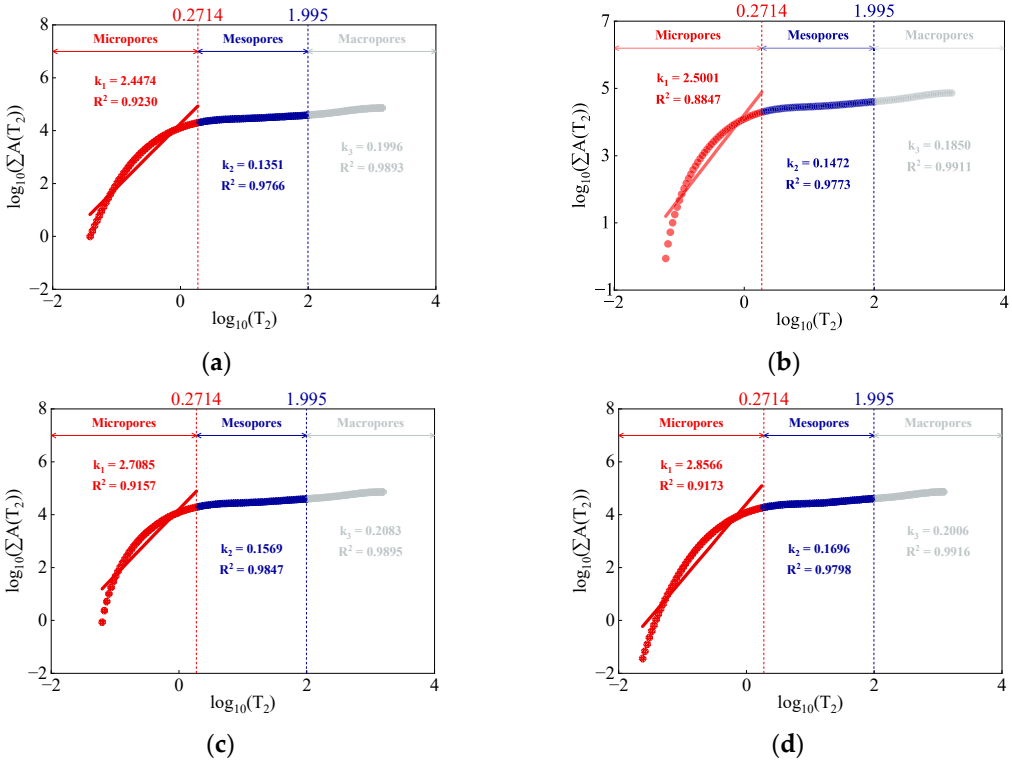


Figure 14. Pore-scale classification and evolution of Core #4. (**a**) 0 PV; (**b**) 100 PV; (**c**) 500 PV; and (**d**) 1000 PV. The symbol "#" indicates the identification number of each core sample.

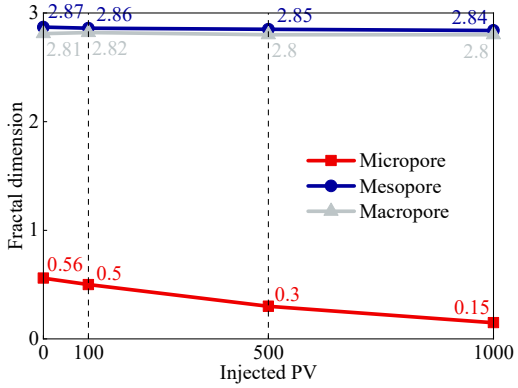


Figure 15. Fractal dimension evolution of multi-scale pores in Core #4. The symbol "#" indicates the identification number of each core sample.

4.3. Spatial Evolution Patterns of Pore Structure During Prolonged Water Injection

Under prolonged water injection, the spatial evolution of pore structures in loosely consolidated sandstones exerts a significant influence on water injection efficiency and fluid distribution. In this study, continuous NMR monitoring was conducted at multiple

positions along the cores from the injection end, systematically revealing the response characteristics of pore structures along the flow direction and their stage-wise evolution.

Figure 16 illustrates the evolution of total NMR signals at different positions within each core during prolonged water injection. In the initial stage (0–100 PV), the signal decrease is most pronounced near the injection end, ranging from approximately 11.2% to 18.4%, whereas the distal end exhibits a more modest decline of 2.9–12.4%. This indicates that fluid perturbation is initially concentrated near the injection site, forming localized preferential flow channels, while responses at the distal end lag. During the intermediate stage (100–500 PV), NMR signals exhibit a rebound, reflecting a redistribution of flow pathways within the cores accompanied by adjustments in local connectivity; the rebound is more substantial at the injection end (7.7–21.7%) and less pronounced at the distal end (1.9–17.1%). In the later stage (500–1000 PV), signal variations at all positions are reduced relative to the preceding stages. These observations demonstrate that, throughout prolonged water injection, the pore structure evolution of loose sandstone exhibits marked spatial heterogeneity along the flow direction, with the most significant changes occurring near the injection end and delayed responses at the distal end.

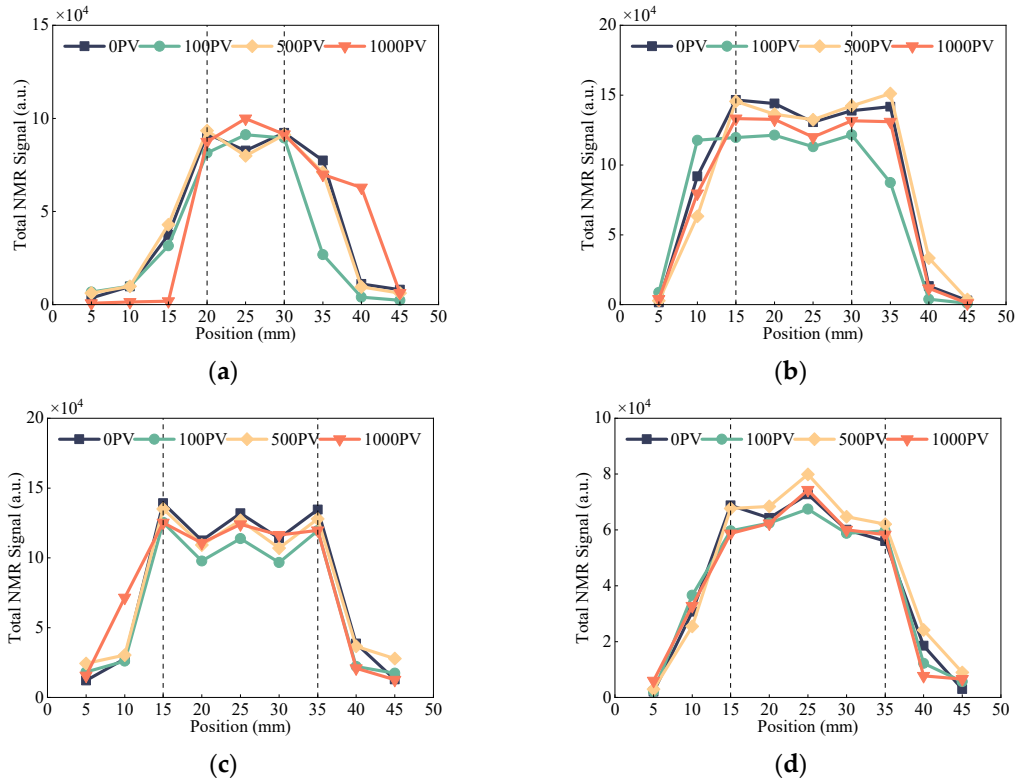


Figure 16. Variation in total NMR signal at different core positions. (**a**) Core #1; (**b**) Core #2; (**c**) Core #3; and (**d**) Core #4. The symbol "#" indicates the identification number of each core sample.

5. Conclusions

To address the lack of multidimensional quantitative analyses of pore structure evolution, this study systematically investigates unconsolidated sandstones under prolonged water injection using multi-scale experiments. Core mineralogy and micro-morphology before and after injection were compared via SEM and XRD, while online NMR monitored the process in real time. Pore sizes were classified based on T_2 spectra, and fractal dimensions were calculated to quantify structural complexity. Total NMR signals along the injection path were further analyzed to reveal the spatially heterogeneous pore response. The main conclusions are as follows:

(1) During prolonged water injection, the liquid-measured permeability of unconsolidated sandstone cores decreased by 10.4–32.1%, while porosity changes remained minor, indicating that the reduction in flow capacity is primarily attributed to pore-throat structural adjustments rather than a loss of pore volume.
(2) Prolonged water injection induced significant changes in both the mineral composition and pore-throat structure of the four cores. Quartz content increased on average by approximately 5%, while total clay mineral content decreased by about 1.2%, and some Plagioclase fractions exhibited slight reductions. Kaolinite and Chlorite contents generally increased, whereas Illite and I/S mixed-layer minerals decreased in certain cores. Microscopic observations indicated adjustments in grain surfaces and pore-throat structures, primarily manifested as redistribution of clay minerals and localized grain-edge dissolution.
(3) Prolonged water injection primarily induces adjustments in the micropore system, exhibiting a pronounced permeability-dependent response, whereas mesopore and macropore structures remain largely stable. Upon completion of water injection, the median pore radius of the cores decreased by 21.5–51.8%. The D_{micro} values of Core #1, #2, #3, and #4 decreased by 23.8%, 76.5%, 61.1%, and 73.2%, respectively, with the magnitude of variation increasing with permeability, indicating that the micropore systems in higher-permeability cores respond more strongly to fluid perturbations during prolonged water injection. In contrast, variations in D_{meso} and D_{macro} are minimal, reflecting only limited local geometric adjustments, and their structural stability remains essentially independent of permeability.
(4) During the initial and intermediate stages of water injection, the NMR signal changes at the injection-end were 11.2–18.4% and 7.7–21.7%, respectively, both exceeding those at the distal end (2.9–12.4% and 1.9–17.1%). In the later stage, signal variations at all positions diminished. These results indicate that, during prolonged water injection, the pore structure evolution of unconsolidated sandstone exhibits pronounced spatial heterogeneity along the flow direction, with the most significant changes occurring near the injection end and delayed responses at the distal end.

Author Contributions: Writing—original draft, H.L. (Hongzhu Li); Investigation, H.L. (Haifeng Lyu); Methodology, Z.G.; Validation, T.S.; Conceptualization, W.Z.; Writing—review and editing, D.K. All authors have read and agreed to the published version of the manuscript.

Funding: This work was supported by the National Natural Science Foundation of China (52574027).

Data Availability Statement: Data are contained within the article.

Acknowledgments: During the preparation of this work the authors used **ChatGPT (GPT-5.3, OpenAI)** in order to improve language. After using this tool, the authors reviewed and edited the content as needed and take full responsibility for the content of the publication.

Conflicts of Interest: Author Haifeng Lyu is employed by the company Petro China Xinjiang Oilfield Company. Authors Zhaobo Gong and Taotao Song are employed by the company Branch Supervision Center of Xinjiang Oilfield Co., Ltd. The remaining authors declare that the research was conducted in the absence of any commercial or financial relationships that could be construed as a potential conflict of interest.

Appendix A

Figures A1–A4 show the evolution of T_2 spectra at multiple positions along Core #1–#4 during prolonged water injection. Due to data quality screening, the effective analytical ranges were 20–30 mm for Core #1, 15–30 mm for Core #2, and 15–35 mm for Core #3

and Core #4. Within these ranges, NMR responses were reproducible and suitable for characterizing spatial pore-structure evolution.

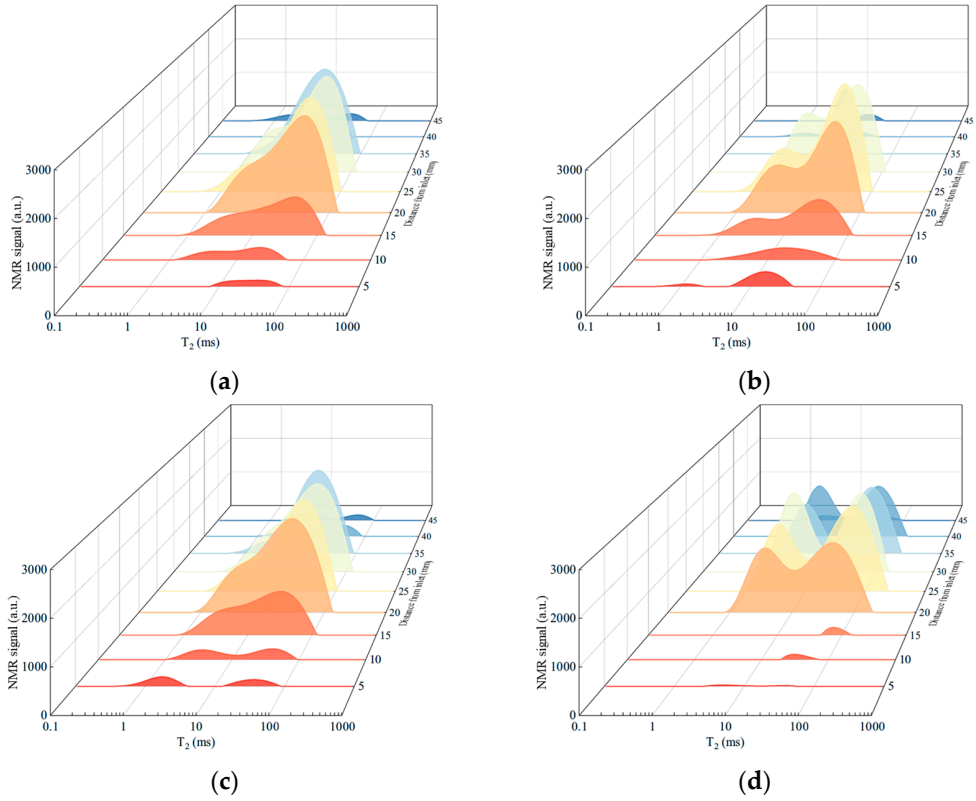


Figure A1. T_2 spectra at different core locations of Core #1 during prolonged water injection. (**a**) 0 PV; (**b**) 100 PV; (**c**) 500 PV; and (**d**) 1000 PV.

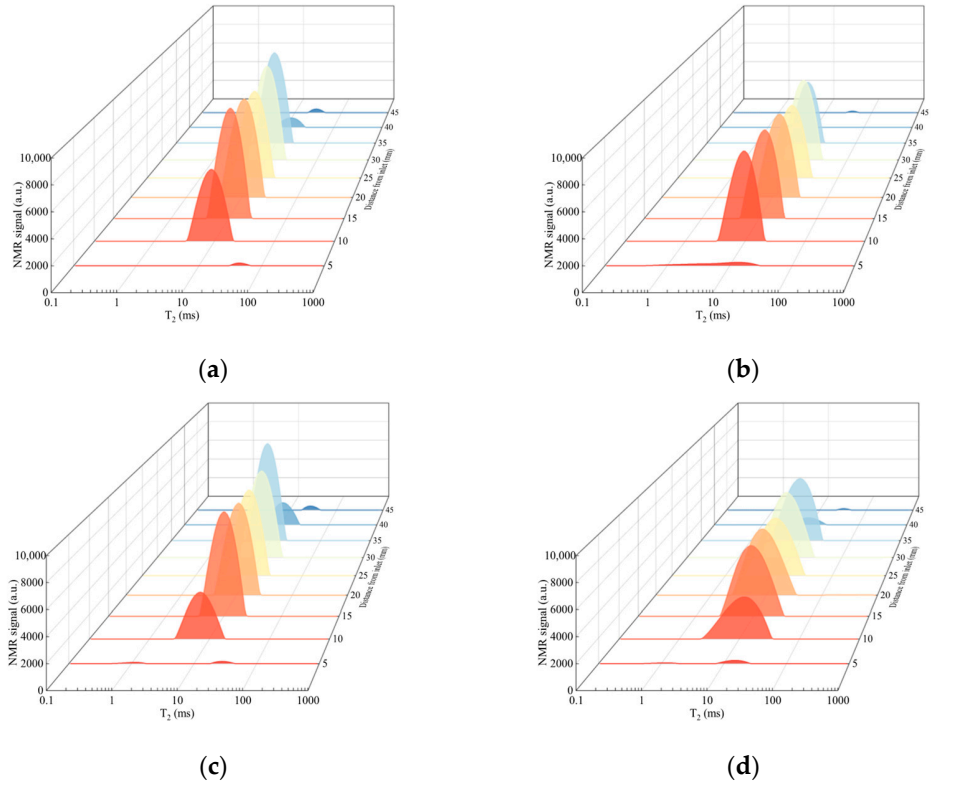


Figure A2. T_2 spectra at different locations of Core #2 during prolonged water injection. (**a**) 0 PV; (**b**) 100 PV; (**c**) 500 PV; and (**d**) 1000 PV.

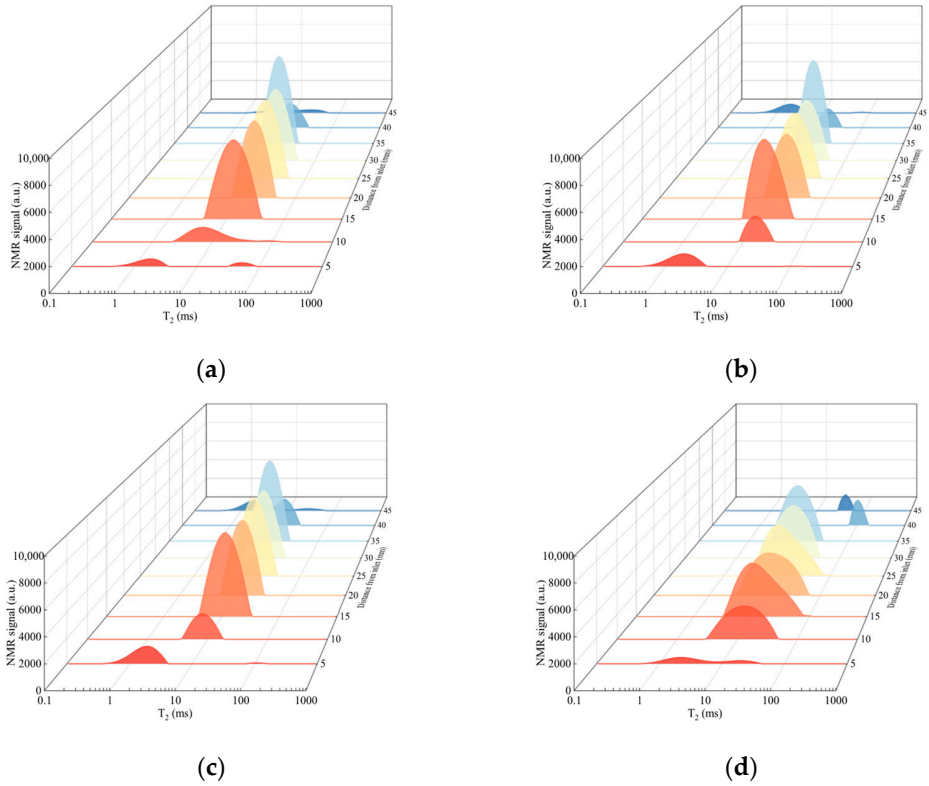


Figure A3. T_2 spectra at different core locations of Core #3 during prolonged water injection. (**a**) 0 PV; (**b**) 100 PV; (**c**) 500 PV; and (**d**) 1000 PV.

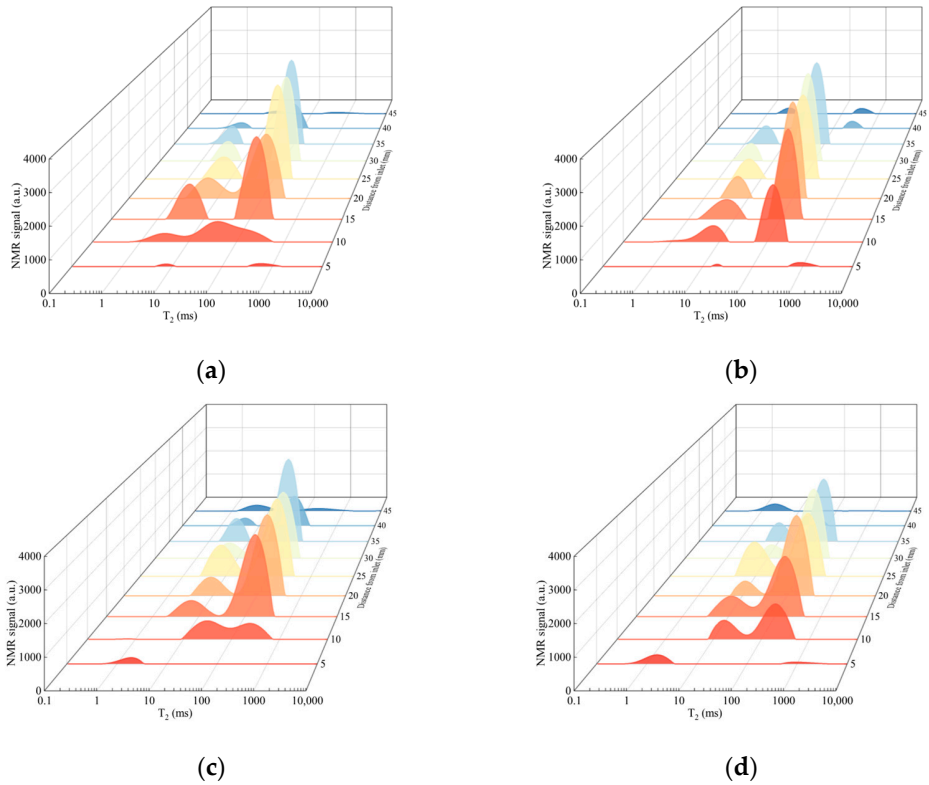


Figure A4. T_2 spectra at different core locations of Core #4 during prolonged water injection. (**a**) 0 PV; (**b**) 100 PV; (**c**) 500 PV; and (**d**) 1000 PV.

References

1. Gao, H.; Liu, Y.; Zhang, Z.; Niu, B.; Li, H. Impact of Secondary and Tertiary Floods on Microscopic Residual Oil Distribution in Medium-to-High Permeability Cores with NMR Technique. *Energy Fuels* **2015**, *29*, 4721–4729. [CrossRef]
2. Tang, H.; Jia, C.; Wang, Z.; Lu, H.; Wang, Z.; Tang, H.; Zhu, B. Evolution of Pore Structure during Fines Migration in Sand Pack: NMR Experimental and Numerical Investigations. *Front. Energy Res.* **2024**, *12*, 1399477. [CrossRef]
3. Wu, S.-F.; Zhang, Y.-F.; Zhao, Y.; Wang, C.-L.; Bi, J.; Long, A.-F.; Li, Y. Real-Time NMR Investigation of Water Infiltration Mechanisms and Pore Structure Evolution in Fractured Sandstone near-Wellbore Regions. *Pet. Sci.* **2025**, *22*, 4195–4210. [CrossRef]
4. Wang, X.; Mao, L.; Kong, X. Microscopic Effects of Long-Term Water Injection on Reservoir Pore Structure. *Geoenergy Sci. Eng.* **2025**, *253*, 213952. [CrossRef]
5. Song, R.; Wang, Y.; Liu, J. Microscopic Pore Structure Characterization and Fluids Transport Visualization of Reservoir Rock. *J. Southwest Pet. Univ. (Sci. Technol. Ed.)* **2018**, *40*, 85–105. [CrossRef]
6. Liu, J.; Li, H.; Xu, J.; Liu, S.; Liu, R.; Hou, L.; Tan, Q. Exploring the Unique Characteristics of High-Pore-Volume Waterflooding and Enhanced Oil Recovery Mechanisms in Offshore Sandstone Reservoirs Using Nuclear Magnetic Resonance Technology. *J. Mar. Sci. Eng.* **2023**, *11*, 1296. [CrossRef]
7. Mansouri, M.; Nakhaee, A.; Pourafshary, P. Effect of SiO_2 Nanoparticles on Fines Stabilization during Low Salinity Water Flooding in Sandstones. *J. Pet. Sci. Eng.* **2019**, *174*, 637–648. [CrossRef]
8. Wang, W.; Li, X.; Wei, Z.; Xin, Y.; Xiao, R.; Yang, H.; Chen, X. Effect of CO_2–Brine–Rock Interactions on the Pore Structure of the Tight Sandstone during CO_2 Flooding: A Case Study of Chang 7 Member of the Triassic Yanchang Formation in the Ordos Basin, China. *ACS Omega* **2023**, *8*, 3998–4009. [CrossRef]
9. Du, M.; Yang, Z.; Lv, W.; Xiao, Q.; Xiang, Q.; Yao, L.; Feng, C. Experimental Study on Microscopic Production Characteristics and Influencing Factors during Dynamic Imbibition of Shale Reservoir with Online NMR and Fractal Theory. *Energy* **2024**, *310*, 133244. [CrossRef]
10. Chen, S.; Yu, H.; Fan, W.; Arif, M. Micro-CT Based Observations of Pore Structure in Tight Sandstone and Residual Oil under CO_2 and Water Flooding. *Fuel* **2026**, *410*, 137764. [CrossRef]
11. Mukunoki, T.; Miyata, Y.; Mikami, K.; Shiota, E. X-Ray CT Analysis of Pore Structure in Sand. *Solid Earth* **2016**, *7*, 929–942. [CrossRef]
12. Yang, Y.; Xiao, W.; Bernabe, Y.; Xie, Q.; Wang, J.; He, Y.; Li, M.; Chen, M.; Ren, J.; Zhao, J.; et al. Effect of Pore Structure and Injection Pressure on Waterflooding in Tight Oil Sandstone Cores Using NMR Technique and Pore Network Simulation. *J. Pet. Sci. Eng.* **2022**, *217*, 110886. [CrossRef]
13. Lyu, C.; Ning, Z.; Wang, Q.; Chen, M. Application of NMR T2 to Pore Size Distribution and Movable Fluid Distribution in Tight Sandstones. *Energy Fuels* **2018**, *32*, 1395–1405. [CrossRef]
14. Li, Y.; Jiang, G.; Li, X.; Yang, L. Quantitative Investigation of Water Sensitivity and Water Locking Damages on a Low-Permeability Reservoir Using the Core Flooding Experiment and NMR Test. *ACS Omega* **2022**, *7*, 4444–4445. [CrossRef]
15. Lin, L.; Xu, C.; Lyu, H.; Chen, Y.; Cong, S.; Yang, X.; Bu, W. Property Changes of Low-Permeability Oil Reservoirs Under Long-Term Water Flooding. *Processes* **2024**, *12*, 2317. [CrossRef]
16. Wen, H.; Liu, Y.; Sun, N. Study on Microheterogeneity and Seepage Law of Reservoir after Long-Term Water Flooding. *J. Pet. Explor. Prod. Technol.* **2017**, *7*, 933–946. [CrossRef]
17. Wang, H.; Zhou, Q.; Sheng, J.; Luo, Y.; Liu, J.; Liu, X. Effect of Long-Term Infiltration on Porosity-Permeability Evolution in Carbonate Rocks: An Online NMR Coupling Penetration Test. *J. Hydrol.* **2023**, *617*, 129029. [CrossRef]
18. Zhang, Y.; Nishizawa, O.; Kiyama, T.; Chiyonobu, S.; Xue, Z. Flow Behaviour of Supercritical CO_2 and Brine in Berea Sandstone during Drainage and Imbibition Revealed by Medical X-Ray CT Images. *Geophys. J. Int.* **2014**, *197*, 1789–1807. [CrossRef]
19. Xu, L.; Cai, M.; Dai, Z.; Zheng, Z.; Chen, W.; Yin, S.; Zhang, X.; Thanh, H.V.; Soltanian, M.R. Fractal and NMR Based Characterizations of Multi-Scale Pore Structure Alterations in Tight Sandstones Due to $scCO_2$-Water–Rock Interactions. *Chem. Eng. J.* **2025**, *508*, 160898. [CrossRef]
20. Li, T.; Fu, M.; Wang, R.; Deng, Y.; Xu, J.; Guo, R. Fractal and Fluid Mobility Analysis of Pore-Throat Systems in Sandstone Reservoirs Based on HPMI and NMR: A Case Study from the Nahr Umr Formation, Iraq. *Fractal Fract.* **2025**, *10*, 15. [CrossRef]
21. Guo, X.; Huang, Z.; Zhao, L.; Han, W.; Ding, C.; Sun, X.; Yan, R.; Zhang, T.; Yang, X.; Wang, R. Pore Structure and Multi-Fractal Analysis of Tight Sandstone Using MIP, NMR and NMRC Methods: A Case Study from the Kuqa Depression, China. *J. Pet. Sci. Eng.* **2019**, *178*, 544–558. [CrossRef]
22. *SY/T5163-2018*; Oil and Gas Industry Standard of the P.R.China: Analysis Method for Clay Minerals and Ordinary Non-Clay Minerals in Sedimentary Rocks by the X-Ray Diffraction. National Energy Administration: Beijing, China, 2019.
23. *GB/T29172-2012*; Practices for Core Analysis. SAC: Beijing, China, 2012.

24. *SY/T 5162-2021*; The Petroleum Industry Standard of China—Analytical Method for Rock Samples by Scanning Electron Microscope. Petroleum Industry Press: Beijing, China, 2022.
25. Li, M.; Qu, Z.; Wang, M.; Ran, W. The Influence of Micro-Heterogeneity on Water Injection Development in Low-Permeability Sandstone Oil Reservoirs. *Minerals* **2023**, *13*, 1533. [CrossRef]

Disclaimer/Publisher's Note: The statements, opinions and data contained in all publications are solely those of the individual author(s) and contributor(s) and not of MDPI and/or the editor(s). MDPI and/or the editor(s) disclaim responsibility for any injury to people or property resulting from any ideas, methods, instructions or products referred to in the content.